Research Article | Vol. 31, No. 16 / 31 Jul 2023 / Optics Express 25915
Optics EXPRESS

Accurate simulation of THz generation with finite-element time domain methods

NILS MARGENBERG,[1,*] FRANZ X. KÄRTNER,[2,3] AND MARKUS BAUSE[1]

[1]Helmut Schmidt University, Faculty of Mechanical and Civil Engineering, Holstenhofweg 85, 22043 Hamburg, Germany
[2]Center for Free Electron Laser Science (CFEL), Deutsches Elektronen-Synchrotron (DESY) & Department of Physics, University of Hamburg, Notkestraße 85, 22607 Hamburg, Germany
[3]The Hamburg Center for Ultrafast Imaging, Luruper Chaussee 149, 22761 Hamburg, Germany
*margenbn@hsu-hh.de

Abstract: We investigate the accurate full broadband simulation of complex nonlinear optical processes. A mathematical model and numerical simulation techniques in the time domain are developed to simulate complex nonlinear optical processes without the usual used slowly varying envelope approximation. We illustrate the accuracy by numerical simulations. Furthermore, they are used to elucidate THz generation in periodically poled Lithium Niobate (PPLN) including optical harmonic generation.

1. Introduction

Nonlinear optical phenomena are the basis of a wide range of applications such as novel optical sources and measurement or diagnostic techniques. With the increasing availability of high-intensity lasers, this field of research progresses fast, continuously uncovering new applications. With growing complexity, however, the simulation of nonlinear optical phenomena becomes more important to achieve optimal performance and save cost and time required for empirical studies.

In recent years wave phenomena have received increasing attention from the applied mathematics community. Nevertheless, scientists or practitioners oftentimes still rely on ad hoc approximations to deal with the central issues that they face. Oftentimes these approximations allow for increased speed but reduce the accuracy of simulations and predictions. We want to demonstrate the accuracy and efficiency of the concepts developed in the field of applied mathematics and apply it to problems of practical interest. In the long term, we hope that this will reduce the need for simplifying assumptions, for example the slowly varying envelope approximation and increase physical realism.

In this work we present efficient and accurate methods for modelling complex phenomena in nonlinear optics. In particular we study frequency mixing processes in the context of THz generation in periodically poled nonlinear crystals by means of Quasi-Phase-Matching. The conceptual basis is the direct simulation of the wave equation, which allows general combinations of dispersion models, nonlinearities and reduced simplifying assumptions. Together with a formulation of a perfectly matched layer (PML) for the domain truncation this allows simulations of phenomena in nonlinear optics with high accuracy. The discretization is done with a finite element time domain (FETD) method with which we gain flexibility w. r. t. complex domain geometries, order of approximation and better handling of discontinuities compared to, e.g., finite differences. We develop our FETD method within the framework of space time finite element methods (STFEM). The computational effort can become enormous, which we alleviate by using

#480793 https://doi.org/10.1364/OE.480793
Journal © 2023 Received 21 Nov 2022; revised 8 Mar 2023; accepted 26 Mar 2023; published 20 Jul 2023

Optics EXPRESS

parallelization and state of the art computational frameworks. We present numerical results for the problem of THz generation in PPLN which demonstrates the accuracy and efficiency of the presented methods. We conclude our work by giving an outlook for future work.

2. Related works

Among the most popular methods to simulate electromagnetic phenomena are finite element methods. There is a wide range of literature and software on them, which we briefly review here. Finite element methods are often used for physical simulations of any kind. In the field of numerical methods for electromagnetics and optics the FETD method [1] allows fully broadband simulations. The FETD method is well established, cf. [1], references therein and [2] for more recent results. However, its use in the field of nonlinear optics results remain sparse: In [3–5] Abraham et al. developed methods for applications similar to the ones studied within this paper. In [6] they extended these methods to a mixed finite element formulation. In [7] the authors use discontinuous Galerkin methods, which can be advantageous for hyperbolic problems due to low dispersion and dissipation errors [8].

In particular, no literature is available on the subject of this paper, finite element time domain methods for the simulation of nonlinear optical generation of THz radiation. In [9–11] the authors use finite difference methods for the spatial discretization and explicit Runge-Kutta methods for the time discretization to simulate simplified models based on the slowly varying envelope approximation. To increase physical realism, we develop a new approach using finite element time domain methods.

In the experimental context the generation of THz radiation is an active field of research with a wide range of applications including imaging [12], linear and nonlinear THz spectroscopy [13] and powering novel accelerators for compact electron sources. In the past, research in nonlinear optical generation of THz radiation has focused on the development of broadband, single-cycle sources [14,15]. These techniques enabled conversion efficiencies approaching 2% [16]. Emerging applications, such as THz-driven electron acceleration [17], require high-field pulses with high spectral purity. This demand has driven multiple advancements, which improved efficiencies from the 1.00×10^{-5} to 1.00×10^{-3} range and THz pulse energies from the nJ to the mJ range [18–21].

Electromagnetic phenomena can be complex, so simplifying assumptions such as considering only a single frequency component (time-harmonic waves) or linear and instantaneously responding materials are popular. Here we consider the dispersive and nonlinear electromagnetic wave equations in the time domain. This gives us the ability to resolve all frequencies while taking frequency dependent responses into account.

In numerical simuations, wave propagation and other physical processes have to be truncated to bounded regions. Artificial boundaries that do not perturb the wave propagation and lead to unphysical reflections, caused by boundary conditions imposed there, are desired. To this end, we discuss an implementation of the PML, which has been introduced in [22]. The PML method is cost-effective, easy to implement and not limited with respect to the computational domain. The original PML formulation relies on a splitting of the physical field into different components. The splitting introduces two different sets of equations in the physical and PML domain. This requires the treatment of the interface between the two domains. An alternative approach is to consider the PML in the frequency domain as a coordinate stretching [23]. From these formulations, a time dependent PML can be derived. The arising convolutions can be computed by means of auxiliary differential equations.

The PML method has been applied to lots of problems in electromagnetics and optics [22,24–49]. Here we will adapt the complex frequency shifted PML (CFS-PML). The advantage of CFS-PML is the ability to account for a wider variety of frequency ranges [50–56]. This is useful for low frequency waves, where the PML is known to fail [46]. For an in-depth review of

Optics EXPRESS

the PML technique we refer to [57] and references therein. An additional issue in nonlinear optics is the treatment of the nonlinear term in the PML region and at the boundary to the physical region. In contrast to this work where the PML is left linear, Abraham et al. [3] kept the PML nonlinear.

We develop the complex frequency PML in the context of space time finite element methods (STFEM) [58]. This allows to use a variety of time stepping methods, for example advantageous higher order methods such as [59]. Variational time discretizations can be seen as a natural extension of variational discretizations in space. This facilitates the use of concepts such as duality and goal oriented adaptivity [60,61]. The concepts of variational space time discretization are also applied to stability and error analysis [62]. Furthermore, the use of space time FEM allow us to solve the wave equation together with the arising auxiliary differential equations (ADE) in a single holistic framework. This framework can then be extended by the methods mentioned above in a generic manner.

3. Mathematical and physical problem

In this section we address the physical models for the propagation of electromagnetic waves in nonlinear dispersive media. Dispersive and nonlinear effects are the result of the wave interacting with the atoms or molecules in a medium. The polarization captures these interactions on a macroscopic level. The polarization P is generally developed as a power series w. r. t. the electric field E with the electric susceptibilities $\chi^{(n)}$. For the materials we consider the linear and quadratic term

$$P = \varepsilon_0 \left(\chi^{(1)} E + \chi^{(2)} E^2 \right) \tag{1}$$

suffices. With the assumptions made above, this expansion of P_i simplifies to (1). In general the coefficients $\chi^{(n)}$ are frequency dependent tensors of $(n+1)$th rank. Linear dispersion can then be described by a frequency dependent $\chi^{(1)}$, as we will do later. While this can also be true for the nonlinear terms, we consider instantaneous nonlinearities in this work. With one exception, we consider homogeneous materials. We assume that $\chi^{(1)}$ and $\chi^{(2)}$ can be simplified to scalar functions. We will discuss concrete functions in later sections. Note that, in the multidimensional case, the polarization P reads as $P_i = \varepsilon_0 \left(\chi^{(1)}_{ij} E^j + \chi^{(2)}_{ijk} E^j E^k \right)$ using Einstein summation convention. The indices range from 1 to d, the number of space dimensions.

3.1. Physical model

We state the governing equations in the time domain where we transform the equations and quantites by applying a time transformation $\tilde{t} = c_0 t$. We use this everywhere and omit the "˜" nomenclature from now on. Let $\mathcal{D} \subset \mathbb{R}^d$ and $I = (0, T]$ be an open bounded time interval. We state the electromagnetic wave equation that includes a second order instantaneous nonlinearity in dispersive media:

$$-\Delta E + \partial_{tt}(n(t)^2 * E) + \chi^{(2)} \partial_{tt} E^2 = f \quad \text{in } \mathcal{D} \times I, \tag{2a}$$

$$E(0) = E_0, \quad \partial_t E(0) = A_0 \quad \text{in } \mathcal{D}, \quad E = g^E \text{ on } \partial\mathcal{D} \times I\,. \tag{2b}$$

A Lorentz dispersion model accounts for the frequency dependent refractive index. It models electrons as damped harmonical oscillators bound to the nucleus. The reaction of an electron to external electromagnetic fields is then given by the differential equation

$$m\ddot{p} + m\Gamma_0 \dot{p} + m\nu_t^2 p = -eE\,. \tag{3}$$

Here m is the electron mass, Γ_0 is the damping coefficient and ν_t is the phonon frequency that raises the refractive index for the low frequencies. We use n_Ω and n_ω as low and high frequency

Optics EXPRESS

limits of the refractive index. The electric permittivity and refractive index can then be expressed through the solution to (3) above:

$$n(\nu)^2 = n_\omega^2 + \frac{(n_\Omega^2 - n_\omega^2)\nu_t^2}{\nu_t^2 - \nu^2 + \mathrm{i}\Gamma_0\nu}\,. \tag{4}$$

In the time domain this leads to the convolution $[n^2 * E](t)$; cf. (2). To avoid the expensive evaluation of the convolution in (2), we derive an ADE. To this end we introduce the auxiliary variable P, which is defined as

$$\frac{(n_\Omega^2 - n_\omega^2)\nu_t^2}{\nu_t^2 - \nu^2 + \mathrm{i}\Gamma_0\nu}E =: P\,. \tag{5}$$

By this definition we obtain $n(\nu)^2 E = n_\omega^2 E + P$ in the frequency domain. The second term of (2) in the frequency domain becomes

$$\partial_{tt}(n(t)^2 * E) = -\nu^2 n_\omega E - \nu^2 P\,. \tag{6}$$

From (5) we derive the ADE for the variable P in the frequency domain

$$\nu_t^2 P - \nu^2 P + \mathrm{i}\Gamma_0\nu P - (n_\Omega^2 - n_\omega^2)\nu_t^2 E = 0\,. \tag{7}$$

We transform (7) to the time domain with an inverse Fourier transform. This leads to the actual ADE (8a) for Lorentz materials in the time domain. We use the ADE (7) to substitute $-\nu^2 P$ in (6) and insert this into the electromagnetic wave Eq. (2), such that we recover (2a) a

$$\partial_{tt}P + \Gamma_0\partial_t P + \nu_t^2 P - (n_\Omega^2 - n_\omega^2)\nu_t^2 E = 0, \tag{8a}$$

$$-\Delta E + n_\omega^2\partial_{tt}E + (n_\Omega^2 - n_\omega^2)\nu_t^2 E - \nu_t^2 P - \Gamma_0\partial_t P + \chi^{(2)}\partial_{tt}(E^2) = 0, \tag{8b}$$

with boundary and initial conditions as given in (2b). The technique of avoiding the evaluation of the convolution by deriving an ADE is well-suited for the space time finite element framework. However, alternative methods for evaluating the convolution have been proposed, most notably the recursive convolution method (RCM) [63–65] and z-transform method [66,67].

In [68] the z-transform has been applied to nonlinear dispersive media. This has proven to be efficient and easily generalizable to complex media, which can be hard to achieve when the ADE method is used. Nevertheless, the ADE method has advantages over the RCM and z-transform approach. Firstly, the ADE will be discretized and solved with the same numerical methods as the actual wave equation. Thus we maintain the same order of approximation for all equations of our model. Furthermore we maintain the high level of flexibility w. r. t. the discretization techniques. This also facilitates error and stability investigations. Secondly, the implementation effort for adding an ADE to an existing space time finite element framework is small.

3.2. Domain truncation

In numerical simuations, wave propagation and other physical studies have to be truncated to bounded regions. Artificial boundaries that do not perturb the wave propagation and lead to unphysical reflections, caused by the imposed boundary conditions, are desired. Two main types of methods exist for the implementation of such types of boundaries.

The first method uses an absorbing boundary condition on the surface of the domain. The waves leave the domain without spurious reflections. In practice these types of boundary conditions are difficult to implement due to their fast growing complexity for higher order methods. Secondly, satisfactory absorption at sharp incident angles independent of the order is not feasible.

The second method used for absorbing boundaries is the PML. It is based on the idea to absorb all waves in an artificial boundary region using a volume surrounding the physical domain. Here we apply the complex frequency shifted PML (CFS-PML) that is based on [55]. It allows us to derive ADEs similar to the Lorentz dispersion, which leads to a high level of flexibility w. r. t. the applications of discretization techniques.

Optics EXPRESS

3.2.1. Complex frequency shifted PML

Complex frequency shifted PML (CFS-PML) are based on a complex stretch of coordinates. As the name suggests, CFS-PML use a frequency-shifted complex coordinate stretching function:

$$s_k(\nu) = \kappa_k + \frac{\sigma_k}{\alpha_k + \mathrm{i}\nu}, \quad k \in x,\, y,\, z\,. \tag{9}$$

The reciprocal of this function will be useful later on:

$$\frac{1}{s_k(\nu)} = \frac{1}{\kappa_k} + \frac{\tilde{\sigma}_k}{\tilde{\alpha}_k + \mathrm{i}\nu}, \quad k \in x,\, y,\, z, \text{ where } \tilde{\sigma_k} = -\frac{\sigma_k}{\kappa_k^2} \text{ and } \tilde{\alpha_k} = \frac{\sigma_k}{\kappa_k} + \alpha_k\,. \tag{10}$$

In general, the parameters are functions depending on the position in the PML. Here we chose a cosine profile

$$f_c = b_c + a_c \left(\frac{1}{2} - \frac{1}{2}\cos\left(2\pi\frac{\mathbf{v}_k}{\delta}\right)\right)^{p_c}, \quad \text{where} \quad c \in \{\alpha_k,\, \sigma_k,\, \alpha_k\}\,. \tag{11}$$

The parameters should be chosen such that $\kappa_k = 1$ and $\sigma_k = 0$ at the interface to the physical domain to ensure continuity of the physical parameters and thereby the continuity of the solutions E and A. The frequency shift α decays from the interface towards the PML boundary. The parameter δ is the thickness of PML and $\mathbf{v}_k$ the distance to the interface to the physical domain.

We derive the ADE formulation of the CFS-PML by multiplying the first term of (8b) by s_x which leads to

$$\partial_x \frac{1}{s_x}\partial_x E + \left(\kappa_x + \frac{\sigma_x}{\alpha_x + \mathrm{i}\nu}\right)\left(n_\omega^2 + \frac{(n_\Omega^2 - n_\omega^2)\nu_t^2}{\nu_t^2 - \nu^2 + \mathrm{i}\Gamma_0\nu}\right)\nu^2 E = 0\,. \tag{12}$$

We need to derive an ADE for the term $\frac{1}{s_x}\partial_x E$ in (12) as well as for the product of s_x and the Lorentz term. For the former we introduce the auxiliary variable Q,

$$\partial_x \frac{1}{s_x}\partial_x E = \partial_x \kappa_x^{-1}\partial_x E + \partial_x \frac{\tilde{\sigma}_x}{\tilde{\alpha}_x + \mathrm{i}\nu}\partial_x E = \partial_x \kappa_x^{-1}\partial_x E + \partial_x Q, \tag{13}$$

where Q is the solution to the equation $\mathrm{i}\nu Q + \tilde{\alpha}_x Q - \tilde{\sigma}_x \partial_x E = 0$. The product of the Lorentz dispersion term is more involved. The product of PML and Lorentz term yields

$$\begin{aligned}\left(\kappa_x + \frac{\sigma_x}{\alpha_x + \mathrm{i}\nu}\right)\left(n_\omega^2 + \frac{(n_\Omega^2 - n_\omega^2)\nu_t^2}{\nu_t^2 - \nu^2 + \mathrm{i}\Gamma_0\nu}\right) = \\ \left(\kappa_x + \frac{\sigma_x}{\alpha_x + \mathrm{i}\nu}\right) n_\omega^2 + \kappa_x \frac{(n_\Omega^2 - n_\omega^2)\nu_t^2}{\nu_t^2 - \nu^2 + \mathrm{i}\Gamma_0\nu} + \frac{\sigma_x}{\alpha_x + \mathrm{i}\nu}\frac{(n_\Omega^2 - n_\omega^2)\nu_t^2}{\nu_t^2 - \nu^2 + \mathrm{i}\Gamma_0\nu}\,.\end{aligned} \tag{14}$$

In the following definition of the equations we do not consider the last term in (14). This avoids the necessity to handle third order time derivatives. Since the parameter σ will always be 0 at the interface between physical and PML region, we don't expect this to have major influence on our model and the accuracy of the simulations. We further limit our model to the one dimensional case.

Definition 3.1 (ADE-CFS-PML equation in 1 dimension with Lorentz dispersion). Let $\mathcal{D} = [0,\, L_\mathcal{D}] \subset \mathbb{R}$ be a closed interval with boundary $\Gamma_D = \{0,\, L_\mathcal{D}\}$ and $I = (0,\, T]$ a bounded time interval. Corresponding to our real test case we prescribe Dirichlet boundary conditions on both endpoints of $\mathcal{D}$. We further define the decomposition of $\mathcal{D}$ into disjoint intervals $\mathcal{D} = \mathcal{D}_{\text{Phy}} \cup \mathcal{D}_{\text{PML}}$. The decomposition is defined by the intervals $\mathcal{D}_{\text{Phy}} = [0,\, L_{\text{Phy}})$ and

Optics EXPRESS

$\mathcal{D}_{\text{PML}} = [L_{\text{Phy}}, L_{\mathcal{D}}]$, where $L_{\text{PML}} = L_{\mathcal{D}} - L_{\text{Phy}}$. The physical region $\mathcal{D}_{\text{Phy}}$ is the domain of physical interest, e.g., the periodically poled crystal in our case. The PML region $\mathcal{D}_{\text{PML}}$ on the other hand purely exists for damping incoming waves. In the physical region Ω_{Phy} the governing equations read as

$$\partial_{tt}P + \Gamma_0\partial_t P + \nu_t^2 P - (n_\Omega^2 - n_\omega^2)\nu_t^2 E = 0, \tag{15a}$$

$$-\Delta E + n_\omega^2\partial_{tt}E + (n_\Omega^2 - n_\omega^2)\nu_t^2 E - \nu_t^2 P - \Gamma_0\partial_t P + \chi^{(2)}\partial_{tt}(E^2) = 0, \tag{15b}$$

with initial conditions $E(x, 0) = E_0(x)$, $x \in \mathcal{D}_{\text{Phy}}$ and boundary conditions $E(x, t) = g(x, t)$, $x = 0$, $t \in (0, T]$. Inside the PML-region Ω_{PML} we solve the equations

$$\partial_{tt}P + \Gamma_0\partial_t P + \nu_t^2 P - \kappa_x(n_\Omega^2 - n_\omega^2)\nu_t^2 E = 0, \tag{16a}$$

$$\partial_t R + \alpha_x R - n_\omega^2\sigma_x E = 0, \tag{16b}$$

$$\partial_t Q + \tilde{\alpha}_x Q - \tilde{\sigma}_x\partial_x E = 0, \tag{16c}$$

$$-\nabla\cdot\kappa_x^{-1}\nabla E + \partial_x Q + \kappa_x n_\omega^2\partial_{tt}E + \kappa_x(n_\Omega^2 - n_\omega^2)\nu_t^2 E \tag{16d}$$

$$-\nu_t^2 P - \Gamma_0\partial_t P + \partial_t\left(n_\omega^2\sigma_x E - \alpha_x R\right) = 0, \tag{16e}$$

with initial conditions $E(x, 0) = 0$, $x \in \mathcal{D}_{\text{PML}}$ and boundary conditions $E(x, t) = 0$, $x = L_{\mathcal{D}}$, $t \in (0, T]$.

4. Discretization

In this section we develop the numerical methods for solving the electromagnetic wave equation introduced in Def. 3.1. First we write the electromagnetic wave equation as a first order in time system.

Problem 4.1 (First order ADE-CFS-PML equation). Considering Eq. (15) given in Def. 3.1. the first order in time governing equations in the physical region $\mathcal{D}_{\text{Phy}}$ are

$$\partial_t P + \Gamma_0 P - U = 0, \tag{17a}$$

$$\nu_t^2 P - (n_\Omega^2 - n_\omega^2)\nu_t^2 E + \partial_t U = 0, \tag{17b}$$

$$n_\omega^2\partial_t E - \Gamma_0 P + \chi^{(2)}\partial_t(E^2) - A = 0, \tag{17c}$$

$$-\Delta E + (n_\Omega^2 - n_\omega^2)\nu_t^2 E - \nu_t^2 P + \partial_t A = 0\,. \tag{17d}$$

Note that we introduced auxiliary variables A and U in order to obtain the first order formulation. The equations inside the PML-region Ω_{PML} can be formulated analogously without changing the equations for Q and R.

4.1. Variational space time methods

We briefly review variational space-time methods along the lines of [58] and investigate discretization in space and time with special focus on the nonlinearity and PML. In addition to the definitions given in Def. 3.1. let $L := L^2(\mathcal{D})$ and $V := H_0^1(\Gamma_D; \mathcal{D})$, where H_0^1 is the space of H^1-functions with vanishing trace on the specified part of the boundary (here Γ_D). For the definition of these function spaces we refer to [69]. We denote the L^2-inner product by $\langle\bullet, \bullet\rangle_\bullet$, where the subscript denotes the domain of integration and $\langle\bullet, \bullet\rangle := \langle\bullet, \bullet\rangle_{\mathcal{D}}$. By $\bullet$ we denote the L^2-norm and by $\|\bullet\|_1$ the H^1-norm. Let $L := L^2(\mathcal{D})$ and $V := H_0^1(\mathcal{D})$. We split the time interval

Optics EXPRESS

I into a sequence of N disjoint subintervals $I_n = (t_{n-1}, t_n]$, $n = 1, \ldots, N$. For a Banach space B and $k \in \mathbb{N}_0$ we define

$$\mathbb{P}_k(I_n, B) = \left\{ w_{\tau_n} : I_n \to B \;\middle|\; w_{\tau_n}(t) = \sum_{j=0}^{k} W^j t^j \forall t \in I_n,\ W^j \in B \forall j \right\}. \tag{18}$$

For $r \in \mathbb{N}$ we define the finite element space that is built on the spatial mesh as

$$\mathcal{V}_h^r = \left\{ v_h \in C(\bar{\mathcal{D}}) \;\middle|\; v_h|_K \in \mathcal{Q}_r(K)\ \forall K \in \mathcal{T}_h \right\} \cap H_0^1(\mathcal{D}), \tag{19}$$

where $\mathcal{Q}_r(K)$ is the space defined by the reference mapping of polynomials on the reference element with maximum degree r in each variable. For the discretization of the equations in (17) we split the time interval I into a sequence of N subintervals I_n. With a discontinuous test basis supported on the subintervals I_n, this leads to a sequence of the following local problems on each subinterval.

Problem 4.2 (Space-time formulation of the ADE-CFS-PML equation). Assume that the trajectories $e_{\tau,h}$, $a_{\tau,h}$, $p_{\tau,h}$ and $u_{\tau,h}$ have been computed before for all $t \in [0, t_{n-1}]$, starting with initial conditions $e_{\tau,h}(0) = e_{0,h}$, $a_{\tau,h}(0) = a_{0,h}$, $p_{\tau,h}(0) = p_{0,h}$ and $u_{\tau,h}(0) = u_{0,h}$. Consider solving the following local problem on the interval I_n:

For given $e_h^{n-1} := e_{\tau,h}(t_{n-1}) \in \mathcal{V}_h^1$ with $e_{\tau,h}(t_0) := e_{0,h}$, find $(e_{\tau,h}, a_{\tau,h}, p_{\tau,h}, u_{\tau,h}) \in \mathbb{P}_1(I_n, \mathcal{V}_h^1) \times \mathbb{P}_1(I_n, \mathcal{V}_h^1)^3$, such that $e_{\tau,h}(t_{n-1}) = e_h^{n-1}$ and

$$\int_{t_{n-1}}^{t_n} \langle \partial_t p_{\tau,h}, \varphi_{\tau,h} \rangle + \Gamma_0 \langle p_{\tau,h}, \varphi_{\tau,h} \rangle - \langle u_{\tau,h}, \varphi_{\tau,h} \rangle \mathrm{d}t = 0, \tag{20a}$$

$$\int_{t_{n-1}}^{t_n} \nu_t^2 \langle p_{\tau,h}, \varphi_{\tau,h} \rangle - (n_\Omega^2 - n_\omega^2) \nu_t^2 \langle e_{\tau,h}, \varphi_{\tau,h} \rangle + \langle \partial_t u_{\tau,h}, \varphi_{\tau,h} \rangle \mathrm{d}t = 0, \tag{20b}$$

$$\begin{aligned} \int_{t_{n-1}}^{t_n} & n_\omega^2 \langle \partial_t e_{\tau,h}, \varphi_{\tau,h} \rangle - \Gamma_0 \langle p_{\tau,h}, \varphi_{\tau,h} \rangle \\ & + \chi^{(2)} \langle \partial_t (e_{\tau,h} e_{\tau,h}), \varphi_{\tau,h} \rangle - \langle a_{\tau,h}, \varphi_{\tau,h} \rangle \mathrm{d}t = 0, \end{aligned} \tag{20c}$$

$$\begin{aligned} \int_{t_{n-1}}^{t_n} & \langle \nabla e_{\tau,h}, \nabla \varphi_{\tau,h} \rangle + (n_\Omega^2 - n_\omega^2) \nu_t^2 \langle e_{\tau,h}, \varphi_{\tau,h} \rangle \\ & - \nu_t^2 \langle p_{\tau,h}, \varphi_{\tau,h} \rangle + \langle \partial_t a_{\tau,h}, \varphi_{\tau,h} \rangle \mathrm{d}t = \int_{t_{n-1}}^{t_n} f, \end{aligned} \tag{20d}$$

for all $(v_{\tau,h}, w_{\tau,h}, w_{\tau,h}, w_{\tau,h}) \in \mathbb{P}_0(I_n, \mathcal{V}_h^1) \times \mathbb{P}_0(I_n, \mathcal{V}_h^1)^3$. The equations inside the PML region can be derived in an analogous manner with $R \in \mathbb{P}_1(I_n, \mathcal{V}_h^1)$ and $Q \in \mathbb{P}_1(I_n, \mathcal{V}_h^1)$.

We formulate a discrete problem in space and time by expanding the solutions $e_{\tau,h}$, $a_{\tau,h}$, $p_{\tau,h}$, $u_{\tau,h}$ in (20) in terms of temporal basis functions. In this work we consider the lowest order case of linear polynomials.

4.1.1. Linear Galerkin method in time for the wave equation

The representation of $(e_{\tau,h}, a_{\tau,h}, p_{\tau,h}, u_{\tau,h})$ in terms of linear polynomials $\varphi_{n,0}$ and $\varphi_{1,1} \in \mathbb{P}_1(\bar{I}_n; \mathbb{R})$ on $\bar{I}_n$ can be substituted into (20). Then we integrate (20) numerically and get the system of equations

$$\mathcal{M}\mathbf{v}_h^n + \frac{\tau_n}{2}\mathcal{A}\mathbf{v}_h^n = \frac{\tau_n}{2}\left(\mathbf{b}_h^{n-1} + \mathbf{b}_h^n\right) + \mathcal{M}\mathbf{v}_h^{n-1} - \frac{\tau_n}{2}\mathcal{A}\mathbf{v}_h^{n-1}. \tag{21}$$

The solution vectors are defined as $\mathbf{v}_h^n = \left((u_h^n)^\top, (p_h^n)^\top, (e_h^n)^\top, (a_h^n)^\top\right)^\top$. The discrete operators $\mathcal{M}$ and $\mathcal{A}$ are defined in terms of $(\mathcal{M})_{ij} = \langle \varphi_{h,j}, \varphi_{h,i} \rangle$, $(\mathcal{A})_{ij} = \langle \nabla \varphi_{h,j}, \nabla \varphi_{h,i} \rangle$ and the nonlinear

Optics EXPRESS

operator $(\mathcal{N}(e))_{ij} = \langle e\varphi_{h,j},\, \varphi_{h,i}\rangle$ as follows

$$\mathcal{A} = \begin{pmatrix} -\mathcal{M} & \Gamma_0\mathcal{M} & 0 & 0 \\ 0 & \nu_t^2\mathcal{M} & -(n_\Omega^2 - n_\omega^2)\nu_t^2\mathcal{M} & 0 \\ 0 & \Gamma_0\mathcal{M} & 0 & -\mathcal{M} \\ 0 & -\nu_t^2\mathcal{M} & (n_\Omega^2 - n_\omega^2)\nu_t^2\mathcal{M} + \mathcal{A} & 0 \end{pmatrix}, \quad \mathcal{M} = \begin{pmatrix} 0 & \mathcal{M} & 0 & 0 \\ \mathcal{M} & 0 & 0 & 0 \\ 0 & 0 & n_\omega^2\mathcal{M} + \chi^{(2)}\mathcal{N}(e) & 0 \\ 0 & 0 & 0 & \mathcal{M} \end{pmatrix}.$$

The system of Eqs. (21) is equivalent to the one we would get from the well-known Crank-Nicholson method. By deriving update equations for the variables u_h^n, p_h^n and a_h^n we can condense (21) such that we just need to solve for e_h^n.

For the solution of the system of nonlinear Eqs. (21) we use a linearization with a damped version of the Newton method. Let $\mathbf{v}_h^n \in \mathcal{V}_h$: $\mathcal{S}(\mathbf{v}_h^n) = \mathcal{F}$ be the nonlinear system of equations defined by (21). We assume that it is sufficiently differentiable by means of the Gateaux derivative $\mathcal{S}'(\mathbf{v}_h^n;\, \delta\mathbf{v}_h^n) := \frac{\mathrm{d}}{\mathrm{d}s}\mathcal{S}(\mathbf{v}_h^n + \varepsilon\delta\mathbf{v}_h^n)|_{\varepsilon=0}$. $\mathcal{S}'$ denotes the derivative of $\mathcal{S}$ at $\mathbf{v}_h^n \in \mathcal{V}_h$ in direction $\delta\mathbf{v}_h^n \in \mathcal{V}_h$. In each step of the Newton method a linear system of equations arise from the discretization, which can then be solved with linear solvers, e.g., Conjugate Gradient or Multigrid methods. For a general overview of iterative methods see [70] or [71,72] for multigrid methods in particular. Details on the application of Newton's method and its variants to nonlinear partial differential equations can be found in the literature [73,74]. Similar methods for the solution of nonlinear electromagnetic wave equations including dispersive nonlinearities have been developed in [4,68]. They have also been implemented on GPUs [6]. The Newton iteration for solving (21) with an initial guess $\mathbf{v}_{h0}^n \in \mathcal{V}_h$ iterates for $m = 0, \ldots$

$$\delta\mathbf{v}_{hm}^n\colon \mathcal{S}'(\mathbf{v}_{hm-1}^n;\, \delta\mathbf{v}_{hm}^n) = \mathbf{F} - \mathcal{S}(\mathbf{v}_{hm-1}^n), \quad \mathbf{v}_{hm}^n := \mathbf{v}_{hm-1}^n + \delta\mathbf{v}_{hm}^n\,. \tag{22}$$

As we have already seen in (16) the system of equations grow larger in the PML region due to the additional variables for the PML. However, we can condense this system to the same size as for the physical domain by reducing the ADEs to simple update equations. Since we don't consider nonlinear processes inside the PML, the nonlinear part can be left out here. We redefine $\mathbf{v}_h^n$ and the operators $\mathcal{M}$ and $\mathcal{A}$ in the PML region $\mathcal{D}_{\mathrm{PML}}$ as $\mathbf{v}_h^n = \left((q_h^n)^\top, (r_h^n)^\top, (u_h^n)^\top, (p_h^n)^\top, (e_h^n)^\top, (a_h^n)^\top\right)^\top$ and

$$\mathcal{A} = \begin{pmatrix} \tilde{\alpha}G & 0 & 0 & 0 & \tilde{\sigma}\mathcal{A} & 0 \\ 0 & \alpha\mathcal{M} & 0 & 0 & -n_\omega^2\sigma\mathcal{M} & 0 \\ 0 & 0 & -\mathcal{M} & \Gamma_0\mathcal{M} & 0 & 0 \\ 0 & 0 & 0 & \nu_t^2\mathcal{M} & -(n_\Omega^2 - n_\omega^2)\kappa\nu_t^2\mathcal{M} & 0 \\ 0 & -\alpha\mathcal{M} & 0 & -\Gamma_0\mathcal{M} & n_\omega^2\sigma\mathcal{M} & -\mathcal{M} \\ G & 0 & 0 & -\nu_t^2\mathcal{M} & (n_\Omega^2 - n_\omega^2)\kappa\nu_t^2\mathcal{M} + \frac{1}{\kappa}\mathcal{A} & 0 \end{pmatrix}, \quad \mathcal{M} = \begin{pmatrix} \mathcal{G} & 0 & 0 & 0 & 0 & 0 \\ 0 & \mathcal{M} & 0 & 0 & 0 & 0 \\ 0 & 0 & 0 & \mathcal{M} & 0 & 0 \\ 0 & 0 & \mathcal{M} & 0 & 0 & 0 \\ 0 & 0 & 0 & 0 & n_\omega^2\kappa\mathcal{M} & 0 \\ 0 & 0 & 0 & 0 & 0 & \mathcal{M} \end{pmatrix}.$$

Using these definitions, the notation of the system of equations in the PML region doesn't differ compared to (21). Analogous to the equations in the physical region we can derive vector updates for the auxiliary variables. In our numerical investigations in Sec. 5 we study the computational effort required for the PML.

5. Numerical simulation

In this section we demonstrate the efficiency of our techniques and the PML in particular. Firstly, we verify the accuracy of our methods with convergence tests. We chose a test based on plane waves. Secondly, we investigate the physical problem of THz generation in PPLN. We verify

Optics EXPRESS

the methods once again by comparing results and quantities of interest to experimental data. We discuss the practical implications, with a focus on aspects not yet investigated, e.g., second harmonic generation (SHG).

For the implementation we use the finite element toolbox deal.II [75] along with the Trilinos library. These software libraries support parallelization with MPI which is used throughout this work. The nonlinear systems of equations are solved with a Newton-Krylov method. The linear systems of equations arising in each Newton step are solved with the conjugate gradients (CG) method. The convergence is accelerated by the algebraic multigrid solver MueLU [76], that is used as a preconditioner with a single sweep performed for every CG step.

5.1. Convergence and runtime study

Here we verify the numerical methods we developed before. To this end we manufacture a solution by prescribing a function as the solution to (17). We use the residual of this function as a source term, which in turn makes the prescribed function the solution. We use the linear Galerkin method proposed in (21) for the time discretization and the finite element space V_h^2 defined in (19) for the spatial discretization. Consequently, we expect second-order convergence. Although piecewise linear polynomials in space would have been sufficient for ensuring this rate of convergence, we use piecewise quadratic polynomials which has been shown to be advantageous.

We chose a 1D test case in the domain $\mathcal{D} = [0,\ 1.96{\times}10^{-3}]$ over the time interval $I = [0,\ 1.00{\times}10^{-13}]$. As the electric field we chose

$$E(x,\ t) = \sin\left(2\pi\omega_2\left(x - n_2 t\right)\right) + \sin\left(2\pi\omega_1\left(x - n_1 t\right)\right)\ . \tag{23}$$

The source term can be calculated by substituting (23) into (17). To compute the error in the physical domain and exclude error contributions from within the PML region, we introduce a weighting function $l\colon \mathcal{D} \to \mathbb{R}$ that is 1 in the physical domain and 0 in the PML region:

$$l(x) = \begin{cases} 0,\ x \in \mathcal{D}_{\text{PML}}, \\ 1,\ x \in \mathcal{D}_{\text{Phy}}\ . \end{cases}$$

Furthermore we multiply l by the source term to restrict it to the physical domain. Thereby the solution inside $\mathcal{D}_{\text{Phy}}$ is given by (23). Then it propagates into $\mathcal{D}_{\text{PML}}$ where it is attenuated to the point of vanishing.

We study the errors $e_Z = Z(x,\ t) - Z_{\tau,h}(x,\ t)$ for $Z \in \{E,\ A,\ P,\ U\}$ in the norms

$$\|e_Z\|_{L^\infty(L^2)} = \max_{t\in I}\left(\int_{\mathcal{D}} |e_Z|^2 \mathrm{d}x\right)^{\frac{1}{2}}, \qquad \|e_Z\|_{L^2(L^2)} = \left(\int_I \int_{\mathcal{D}} |e_Z|^2 \mathrm{d}x\mathrm{d}t\right)^{\frac{1}{2}}\ . \tag{24}$$

We abbreviate the error quantity $\|e_E\|_{L^\infty(L^2)}$ by $L^\infty - L^2(E)$ and analogously for the other norms and variables. The errors are calculated by simultaneous refinement in space and time. Table 1 and Fig. 1 show the optimal order of convergence we expected, due to the second order convergence in time. This proves the efficacy of our PML implementation and that it is suitable for nonlinear dispersive materials. Towards the end we see a decrease in the order of convergence for the electric field, which is due to minor reflections caused by the PML. This can be avoided at the cost of increased computation time by extending the PML. Here we decided to chose the PML similar to the physical problem we investigate later. We use the convergence test to investigate the influence of the PML on the runtimes and demonstrate the efficiency of the methods used. To this end we compare the computation times per degree of freedom (DoF) inside the PML with those in the physical domain. In order to minimize the computational overhead of the PML we assemble the data structures for the PML once and reuse them in every timestep. This is possible

Optics EXPRESS

since the PML does not have any nonlinearity which needs to be evaluated. For example, the evaluation of the PML damping functions α, σ, κ can become expensive. However, they are time independent and only need to be evaluated once. By caching them the time spent per DoF in the PML increases by less than 1% compared to a DoF in the physical region.

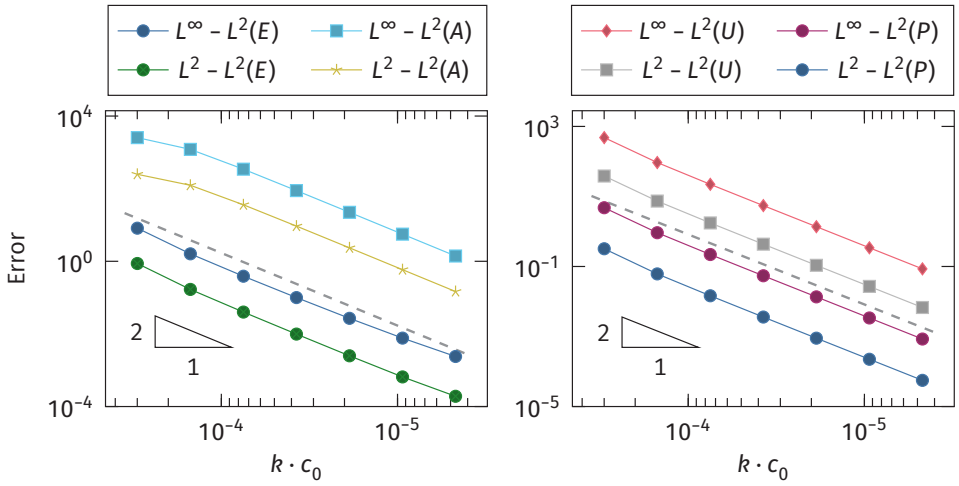

Fig. 1. Calculated errors for the electric field E and the auxiliary variables A, U, P for the linear Galerkin method plotted against the timestep-size. The expected quadratic order of convergence is visualized by the dashed line and the triangles in the lower left corners.

Table 1. Calculated errors and experimental orders of convergence (EOC) for the electric field and the auxiliary variable *A* for the linear Galerkin method introduced in Sec. 4.1.1.

$k \cdot c_0$	$L^\infty - L^2(E)$	EOC	$L^\infty - L^2(A)$	EOC	$L^2 - L^2(E)$	EOC	$L^2 - L^2(A)$	EOC
3.00×10^{-4}	8.16×10^{0}	—	2.55×10^{3}	—	8.69×10^{-1}	—	2.49×10^{2}	—
1.50×10^{-4}	1.61×10^{0}	2.35	1.21×10^{3}	1.08	1.68×10^{-1}	2.37	1.24×10^{2}	1.00
7.49×10^{-5}	3.88×10^{-1}	2.05	3.44×10^{2}	1.81	3.99×10^{-2}	2.07	3.60×10^{1}	1.79
3.75×10^{-5}	1.00×10^{-1}	1.95	8.85×10^{1}	1.96	9.89×10^{-3}	2.01	9.31×10^{0}	1.95
1.87×10^{-5}	2.69×10^{-2}	1.90	2.23×10^{1}	1.99	2.50×10^{-3}	1.99	2.35×10^{0}	1.99
9.37×10^{-6}	7.67×10^{-3}	1.81	5.59×10^{0}	2.00	6.54×10^{-4}	1.93	5.88×10^{-1}	2.00
4.68×10^{-6}	2.39×10^{-3}	1.68	1.40×10^{0}	2.00	1.92×10^{-4}	1.77	1.47×10^{-1}	2.00

This shows that the PML is resource efficient, scales well and the computational overhead is solely determined by the size of the PML. In the following section we briefly analyze the cost of the PML in a realistic setting.

5.2. THz generation in PPLN

In our numerical investigations we simulate THz generation in PPLN. The main goal in this section is to reproduce the experimental results presented in [21]. The simulation data has the advantage that we can evaluate it in all points of the space-time domain. Thus we can correlate the different harmonics with each other and uncover effects of the periodic poling and quasi phase matching. This will improve the understanding of the physical processes. That potentially leads to the improvement of the experimental setup especially for higher intensities where simplified

Optics EXPRESS

models fail. As in [21], we use two pump pulses with super Gaussian envelope

$$g(t) = \exp\left(-\left(2\log 2\left(\tfrac{t}{\tau}\right)^2\right)^P\right)(\cos(2\pi\omega_1 t) + \cos(2\pi\omega_2 t)).$$

The pulses are separated in center frequency by the THz frequency with a full width half maximum $\tau = 2.50\times10^2$ ps and frequencies $\omega_1 = 2.92\times10^2$ THz, $\omega_2 = 2.91\times10^2$ THz and $P = 6$. We chose a pulse with average fluence of 2.00×10^3 J m^{-1}. It is applied at the left-hand side of the crystal by a Dirichlet boundary condition and then propagates through the domain until the PML is hit on the right-hand side. The problem setting is sketched in Fig. 2. The computational effort for these simulations are very high: Depending on the fluence, which influences the number of iterations of the Newton method, the simulations can take up to 4 weeks. The simulations presented here took 3 weeks on a workstation with 2 Intel Xeon E5-2699 CPUs (2×18 cores). In this study, we limited our investigations and numerical simulations to one spatial dimension. This was necessitated by simulation times and the added complexity of using Perfectly Matched Layers (PMLs) in 2D and 3D. In the settings investigated here, the simplification of reducing the simulations to one spatial dimension and neglecting the impacts of the remaining spatial directions is not expected to significantly perturb the results. The simulation results presented here are based on a timestep size of $k = 5.00\times10^{-17}$ and average cell-size of 5.18×10^{-8}, which leads to 1.00×10^{10} number of timesteps and 4.26×10^5 degrees of freedom in space.

The intensities of the simulated results are presented in Fig. 3. We observe, besides the THz radiation generated by difference frequency generation (DFG) in Fig. 3(b), the harmonics in the optical domain in Fig. 3(a). The optical harmonics are simultaneously generated by SHG and sum frequency generation (SFG). In particular the second harmonic near 6.00×10^2 THz and the other nth harmonics can be well observed. At 9.00×10^2 THz we can observe the effect of DFG from the harmonics. The ability to simulate this phenomenon with such a low conversion efficiency again demonstrates the potential and accuracy of the proposed method. We also find significant intensities at frequencies 1.00×10^2 THz, 2.00×10^2 THz and 4.00×10^2 THz cf. 4(a), 3(a).

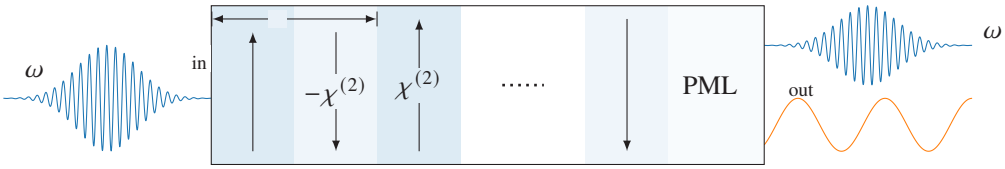

Fig. 2. Example setting of a periodically poled crystal with period Λ. The pump pulse $g(t)$ at frequencies $\omega_{1,2}$ enters the crystal on the left side Γ_{in}. In the subsequent layers THz radiation is generated.

In Fig. 3(c) we show the intensity over the length of the PML at time $t = 2.50\times10^2$ ps when the pulse has entered the crystal. The intensity decays monotonically over the length of the crystal until it almost vanishes. Reflections from the boundary are damped again. Therefore, based on Fig. 3(c) we don't expect spurious reflections into the physical domain. This proves the effectiveness of the formulation of the PML. The PML has the same length as one poling period of the PPLN crystal. With a period of $\Lambda = 2.12\times10^2$ µm and 25 periods the computational domain is enlarged by about 4%. Considering that the increase in computational cost per degree of freedom was about 1% inside the PML in the convergence test, the PML accounts for 4% of the total computing time, which is reasonable.

In Fig. 4(a) we show the internal conversion efficiencies plotted over the whole spectrum from 0.00×10^0 THz to 8.00×10^2 THz. The methods and physical models we use allow us to include nonlinear effects apart from optical to THz conversion in our results. Near 3.00×10^{-1}

Optics EXPRESS

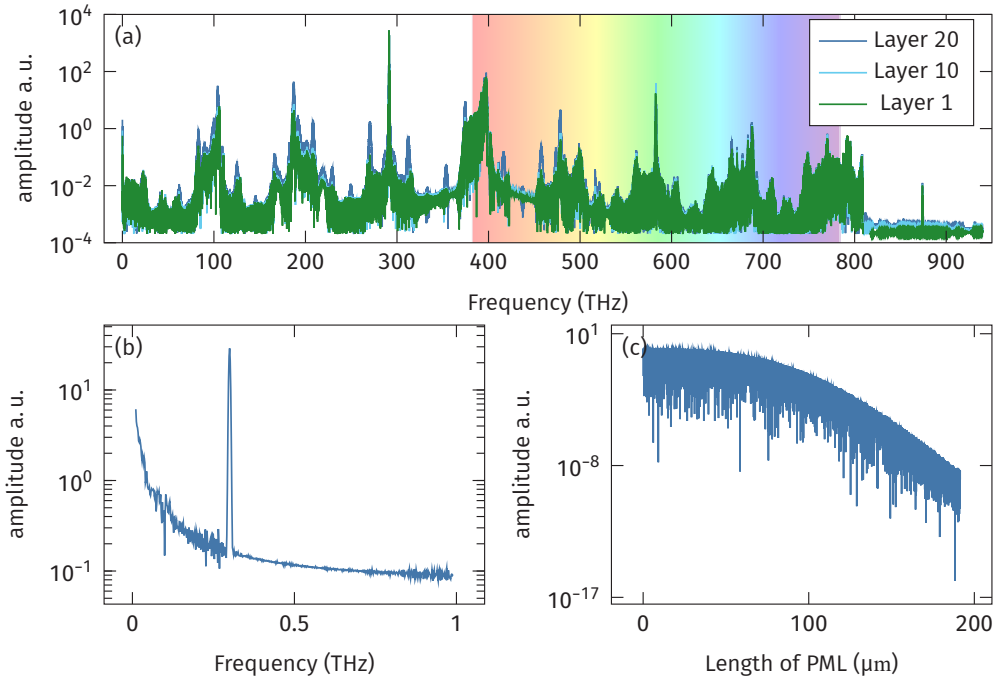

Fig. 3. Plot (a) shows the spectrum of the electromagnetic field after it has passed 25 periods of the crystal shown in Fig. 2 in the 0 THz to 1.00×10^{3} THz region and (b) in the region from 1.00×10^{-2} THz to 1.00×10^{2} THz. Subplot (c) shows the intensity of the electric field inside the PML at time $t = 7.50\times10^{2}$ fs.

THz we see the remaining parts of the two input pulses. We observe a narrow peak near 0THz, corresponding to the generated THz radiation at 3.00×10^{-1} THz. We further see the generation of optical harmonics in a cascading manner. These efficiencies are mostly constant, since these processes are phase-mismatched. For example, the SHG is phase mismatched and nevertheless the conversion efficiencies are of similar magnitude compared to the ones at 3.00×10^{-1} THz. This is due to the much higher efficiency for SHG than for THz generation and despite the large phase mismatch some is generated.

Similar effects can be observed in Fig. 4(a) where the conversion efficiency in the layers are plotted. The conversion efficiency at 4.00×10^{2} THz remains constant over the layers; cf. Figure 4(4). The 3.00×10^{-1} THz radiation on the other hand grows over the layers since the process is phase-matched; cf. Figure 4(1), 4(b). In Fig. 4(2,3) we observe similar phenomena at approximately 1.00×10^{2} THz and 1.90×10^{2} THz. Considering the Lorentz model (4) we note that the phase matching condition for optical parametric oscillation is almost fulfilled for the process of frequency splitting with the pump frequencies ω_1 and ω_2, idler frequency $\omega_i = 1.00\times10^{2}$ THz and respective signal frequencies $\omega_{s,1} = \omega_1 - \omega_i$, $\omega_{s,2} = \omega_2 - \omega_i$.

We conjecture that the significant amount of radiation at 1.00×10^{2} THz and 1.90×10^{2} THz is due to the frequency splitting described above. This hypotheses fits well with the simulation data, where we observe a fast growth of the conversion efficiency. Further, we conjecture that the 4.00×10^{2} THz radiation is a result of frequency mixing processes of the pump, signal and idler frequencies. This corresponds to the observation that there is not a singular peak at one specific frequency but rather multiple frequencies. In the last layers, we see a peak near 3.80×10^{2} THz,

Optics EXPRESS

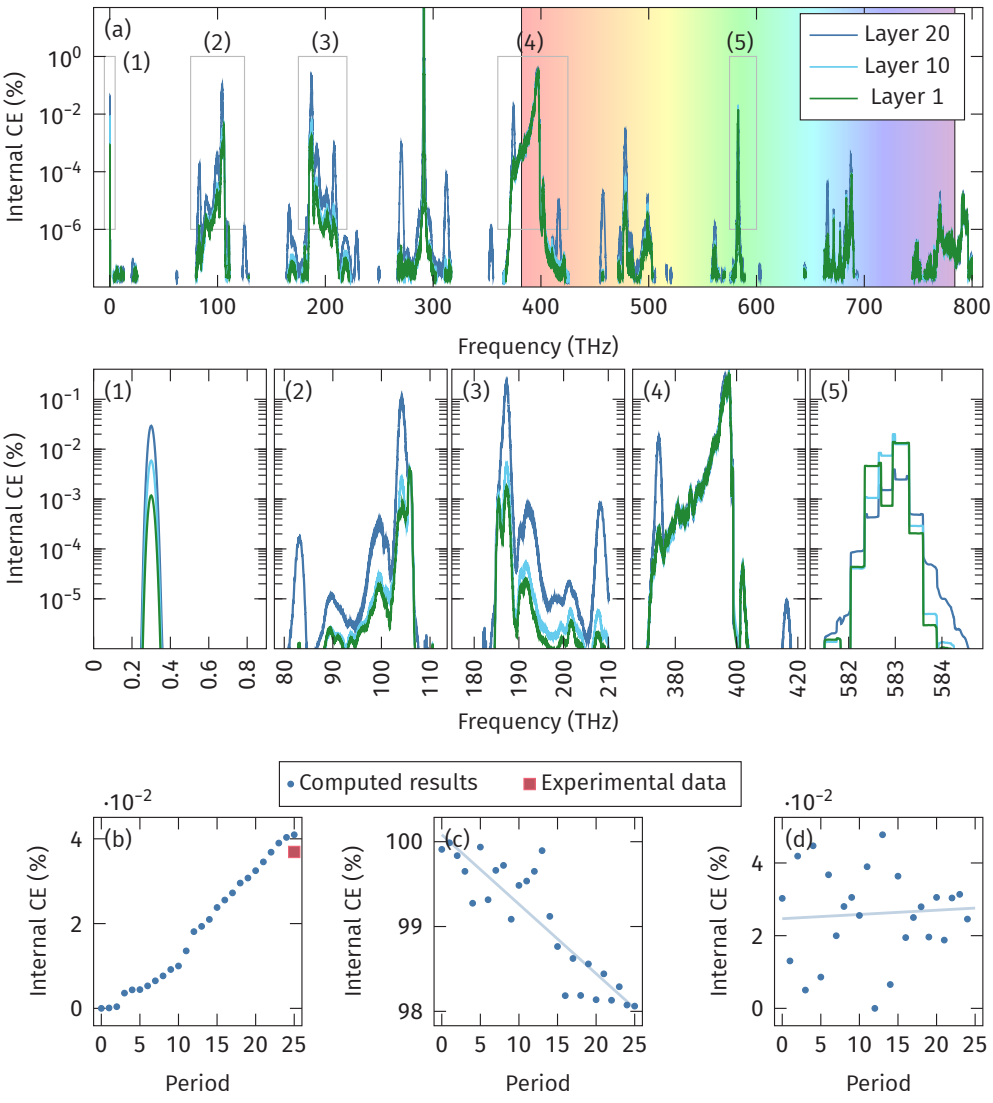

Fig. 4. Internal conversion efficiency (a) for the frequencies from 1.00×10^2 THz to 8.00×10^2 THz. In subplot (b) the intensity at frequencies between 1.00×10^{-1} THz to 1.00×10^0 THz are summed up, then the corresponding conversion efficiencies are plotted over the 25 layers. Subplot (c) shows the conversion efficiencies determined in the same way for frequencies between 1.00×10^2 THz and 8.00×10^2 THz. Subplot (d) shows the conversion efficiencies for the second harmonic. In subplots (c) and (d) the pale blue lines show the linear regression of the data.

Optics EXPRESS

corresponding to the frequency doubling of the signal frequencies $\omega_{s,1}$ and $\omega_{s,2}$. The radiation observed at 4.00×10^2 THz can be attributed to sum frequency generation of ω_i and ω_1 or ω_2.

In Fig. 4(b) we show the development of the internal conversion efficiencies over the layers for the THz spectrum from 1.00×10^{-1} THz to 5.00×10^{-1} THz. We are able to observe a growing THz conversion efficiency, since the process is phase-matched. Furthermore, Fig. 4(b) shows that the simulation data are in good agreement with the experimental data obtained from [21], with a relative error of 9.8 % and an absolute error of 3.90×10^{-3}. Although more work is needed to verify this beyond the results presented here, which are based on a single instance. We interpolated the experimental data between the start of the crystal with 0% conversion efficiency and the end of the crystal, where experimental data are available.

In Fig. 4(c) we show the development of the internal conversion efficiencies over the layers for the spectrum from 1.00×10^2 THz to 8.00×10^2 THz. Experimental data for a comparison in this frequency range was not available. The decay of the conversion efficiency over the layers is physically plausible due to the the optical to THz conversion shown in Fig. 4(b). We note that the conversion efficiencies in Fig. 4(b) and (c) don't necessarily add up to 100% since they don't cover the whole frequency spectrum and we include absorption in the THz range.

In Fig. 4(d) we show the development of the internal conversion efficiencies over the layers from 5.60×10^2 THz to 6.00×10^2 THz, i.e., the second harmonic. We see that the conversion efficiency to the second harmonic doesn't grow significantly. A linear regression reveals that the conversion efficiency increases slowly and stays almost constant on average. The reason for the fluctuations is the phase-mismatch, which leads to oscillating negative and positive interference. This leads to varying conversion efficiencies over the layers, depending on how close we are to a phase-match. This is in contrast to the 3.00×10^{-1} THz radiation in Fig. 4(b), where the processes are phase-matched. It is all the more surprising that we generate so much of the undesired radiation of the second harmonic frequency.

The results presented in Fig. 4 will be used for the optimization of the optical to THz conversion, the validation of simplified simulation algorithms and the development of multiscale models. The validation of the optical parametric oscillation responsible for the generation of 1.00×10^2 THz, 2.00×10^2 THz and 4.00×10^2 THz radiation is subject to future work. Frequency division in PPLN has been used in practice in the past; cf. [77,78]. However, some of the effects observed in the simulations in this work still need to be verified by experiments. In the current model we assumed the refractive index in the optical region at frequencies larger 5.00×10^1 THz as constant. This is not correct and most likely leads to the parametric amplification at 100 and 200 THz, which may not be present in reality. In order to model this wavelength range correctly, the dispersion of the refractive index in the optical wavelength range needs to be implemented. This is beyond the scope of this paper, which is the development of a numerical algorithm for the efficient solution of the nonlinear wave equation.

6. Conclusion

In this work we have simulated THz generation in PPLN. To this end we developed the physical model for nonlinear, dispersive, electromagnetic wave propagation. We investigated the Lorentz dispersion model and absorbing boundary conditions where we derived the governing equations 3.1. We have demonstrated the efficiency of the simulation methods and absorbing boundary conditions that we implemented with the PML. They fit well into the STFEM framework, are effective and increased the computational cost by only 2%. We developed the methods in a framework that is extendable to a wide range of applications within nonlinear optics where numerical methods that are accurate and highly efficient are needed.

In the future we want to extend our code to higher order methods within the STFEM framework to further accelerate the simulations. The higher order methods will allow us to chose larger time steps without the loss of accuracy. This is crucial since simulation times can take up to 4 weeks

Optics EXPRESS

right now. In order to not overburden this presentation, we restricted ourselves to the 1D case. The methods and implementation allow extensions to 2D and 3D and are subject to future work.

Our comparison with experimental data indicated good agreement in terms of the main quantity of interest, the optical to THz conversion efficiency. The fact that we are able to simulate the THz conversion as well as the harmonic generation will allow us to design better effective nonlinear media by poling. We will use the results presented here to optimize the optical to THz conversion further. Future work include studies on this topic. Furthermore a comparison with experimental data obtained from measurements in the optical spectrum is needed to explain and verify the simulation results further. We may need to adjust the dispersion model in the optical wavelength range. In the STFEM framework this can be done with little work and low additional computational cost.

The simulations for the results we present here are computationally feasible but still expensive. The main bottleneck is the time discretization. Since time steps are inherently sequential, the time discretization limits the scalability of parallelization.

Funding. Helmholtz Association (HIDSS-0002).

Acknowledgment. NM acknowledges support by the Helmholtz-Gesellschaft grant number HIDSS-0002 DASHH. The authors would like to thank Prof. Nina Rohringer for the helpful discussions, especially regarding the interpretation of the simulation results.

Disclosures. The authors declare that there are no conflicts of interest related to this article.

Data availability. Data underlying the results presented in this paper are not publicly available at this time but may be obtained from the authors upon reasonable request.

References

1. J. Jin, *The Finite Element Method in Electromagnetics* (Wiley-IEEE Press, 2014), 3rd ed.
2. A. Agrawal, T. Benson, R. M. De La Rue, and G. A. Wurtz, eds., *Recent Trends in Computational Photonics*, no. 204 in Springer Series in Optical Sciences (Springer International Publishing : Imprint: Springer, 2017), 1st ed.
3. D. S. Abraham and D. D. Giannacopoulos, "A Perfectly Matched Layer for the Nonlinear Dispersive Finite-Element Time-Domain Method," IEEE Trans. Magn. **55**(6), 1–4 (2019).
4. D. S. Abraham and D. D. Giannacopoulos, "A Convolution-Free Finite-Element Time-Domain Method for the Nonlinear Dispersive Vector Wave Equation," IEEE Trans. Magn. **55**(12), 1–4 (2019).
5. D. S. Abraham, "Finite-element time-domain methods for nonlinear dispersive media," (2020).
6. D. S. Abraham and D. D. Giannacopoulos, "A Parallel Finite-Element Time-Domain Method for Nonlinear Dispersive Media," IEEE Trans. Magn. **56**(2), 1–4 (2020).
7. Y. Grynko and J. Förstner, "Simulation of Second Harmonic Generation from Photonic Nanostructures Using the Discontinuous Galerkin Time Domain Method," in *Recent Trends in Computational Photonics*, A. Agrawal, T. Benson, R. M. De La Rue, and G. A. Wurtz, eds. (Springer International Publishing, 2017), Springer Series in Optical Sciences, pp. 261–284.
8. J. S. Hesthaven and T. Warburton, *Nodal Discontinuous Galerkin Methods*, vol. 54 of *Texts in Applied Mathematics* (Springer, 2008).
9. K. Ravi, W. R. Huang, S. Carbajo, X. Wu, and F. Kärtner, "Limitations to THz generation by optical rectification using tilted pulse fronts," Opt. Express **22**(17), 20239–20251 (2014).
10. K. Ravi, W. R. Huang, S. Carbajo, E. A. Nanni, D. N. Schimpf, E. P. Ippen, and F. X. Kärtner, "Theory of terahertz generation by optical rectification using tilted-pulse-fronts," Opt. Express **23**(4), 5253–5276 (2015).
11. L. Wang, A. Fallahi, K. Ravi, and F. Kärtner, "High efficiency terahertz generation in a multi-stage system," Opt. Express **26**(23), 29744–29768 (2018).
12. J. P. Guillet, B. Recur, L. Frederique, B. Bousquet, L. Canioni, I. Manek-Hönninger, P. Desbarats, and P. Mounaix, "Review of Terahertz Tomography Techniques," J. Infrared, Millimeter, Terahertz Waves **35**(4), 382–411 (2014).
13. J. Hebling, K.-L. Yeh, M. C. Hoffmann, and K. A. Nelson, "High-power THz generation, THz nonlinear optics and THz nonlinear spectroscopy," in *2008 Conference on Lasers and Electro-Optics and 2008 Conference on Quantum Electronics and Laser Science*, (2008), pp. 1–2.
14. D. Zhang, A. Fallahi, M. Hemmer, X. Wu, M. Fakhari, Y. Hua, H. Cankaya, A.-L. Calendron, L. E. Zapata, N. H. Matlis, and F. X. Kärtner, "Segmented terahertz electron accelerator and manipulator (STEAM)," Nat. Photonics **12**(6), 336–342 (2018).
15. L. Guiramand, J. E. Nkeck, X. Ropagnol, T. Ozaki, and F. Blanchard, "Near-optimal intense and powerful terahertz source by optical rectification in lithium niobate crystal," Photonics Res. **10**(2), 340–346 (2022).
16. A. D. Koulouklidis, C. Gollner, V. Shumakova, V. Y. Fedorov, A. Pugžlys, A. Baltuška, and S. Tzortzakis, "Observation of extremely efficient terahertz generation from mid-infrared two-color laser filaments," Nat. Commun. **11**(1), 292 (2020).

Optics EXPRESS

17. E. A. Nanni, W. R. Huang, K.-H. Hong, K. Ravi, A. Fallahi, G. Moriena, R. J. Dwayne Miller, and F. X. Kärtner, "Terahertz-driven linear electron acceleration," Nat. Commun. **6**(1), 8486 (2015).
18. S. Carbajo, J. Schulte, X. Wu, K. Ravi, D. N. Schimpf, and F. X. Kärtner, "Efficient narrowband terahertz generation in cryogenically cooled periodically poled lithium niobate," Opt. Lett. **40**(24), 5762–5765 (2015).
19. F. Ahr, S. W. Jolly, N. H. Matlis, S. Carbajo, T. Kroh, K. Ravi, D. N. Schimpf, J. Schulte, H. Ishizuki, T. Taira, A. R. Maier, and F. X. Kärtner, "Narrowband terahertz generation with chirped-and-delayed laser pulses in periodically poled lithium niobate," Opt. Lett. **42**(11), 2118–2121 (2017).
20. S. W. Jolly, N. H. Matlis, F. Ahr, V. Leroux, T. Eichner, A.-L. Calendron, H. Ishizuki, T. Taira, F. X. Kärtner, and A. R. Maier, "Spectral phase control of interfering chirped pulses for high-energy narrowband terahertz generation," Nat. Commun. **10**(1), 2591 (2019).
21. H. T. Olgun, W. Tian, W. Tian, G. Cirmi, G. Cirmi, K. Ravi, C. Rentschler, H. Çankaya, H. Çankaya, H. Çankaya, M. Pergament, M. Hemmer, Y. Hua, D. N. Schimpf, N. H. Matlis, and F. X. Kärtner, "Highly efficient generation of narrowband terahertz radiation driven by a two-spectral-line laser in PPLN," Opt. Lett. **47**(10), 2374–2377 (2022).
22. J.-P. Berenger, "A perfectly matched layer for the absorption of electromagnetic waves," J. Comput. Phys. **114**(2), 185–200 (1994).
23. W. C. Chew, J. M. Jin, and E. Michielssen, "Complex coordinate stretching as a generalized absorbing boundary condition," Microw. Opt. Technol. Lett. **15**(6), 363–369 (1997).
24. W. C. Chew and W. H. Weedon, "A 3D perfectly matched medium from modified Maxwell's equations with stretched coordinates," Microw. Opt. Technol. Lett. **7**(13), 599–604 (1994).
25. Z. S. Sacks, D. M. Kingsland, R. Lee, and J. F. Lee, "A perfectly matched anisotropic absorber for use as an absorbing boundary condition," IEEE Trans. Antennas Propagat. **43**(12), 1460–1463 (1995).
26. C. M. Rappaport, "Perfectly matched absorbing boundary conditions based on anisotropic lossy mapping of space," IEEE Microw. Guid. Wave Lett. **5**(3), 90–92 (1995).
27. M. Kuzuoglu and R. Mittra, "Frequency dependence of the constitutive parameters of causal perfectly matched anisotropic absorbers," IEEE Microw. Guid. Wave Lett. **6**(12), 447–449 (1996).
28. J. Y. Wu, D. M. Kingsland, and J. F. L. Lee, "A comparison of anisotropic PML to Berenger's PML and its application to the finite-element method for EM scattering," IEEE Trans. Antennas Propagat. **45**(1), 40–50 (1997).
29. B. Yang, D. Gottlieb, and J. Hesthaven, "Spectral simulations of electromagnetic wave scattering," J. Comput. Phys. **134**(2), 216–230 (1997).
30. S. Abarbanel and D. Gottlieb, "A mathematical analysis of the PML method," J. Comput. Phys. **134**(2), 357–363 (1997).
31. F. L. Teixeira and W. C. Chew, "Advances in the theory of perfectly matched layers," in *Fast and Efficient Algorithms in Computational Electromagnetics*, W. Chew, E. Michielssen, J. M. Song, and J. M. Jin, eds. (Artech House Inc, 2001).
32. F. Collino and P. Monk, "Optimizing the perfectly matched layer," Comput. Methods Appl. Mech. Eng. **164**(1-2), 157–171 (1998).
33. F. Collino and P. Monk, "The perfectly matched layer in curvilinear coordinates," SIAM J. Sci. Comput. **19**(6), 2061–2090 (1998).
34. P. Liu and Y. Q. Jin, "Numerical simulation of bistatic scattering from a target at low altitude above rough sea surface under an EM-wave incidence at low grazing angle by using the finite element method," IEEE Trans. Antennas Propagat. **52**(5), 1205–1210 (2004).
35. S. Abarbanel, D. Gottlieb, and J. S. Hesthaven, "Long time behavior of the perfectly matched layer equations in computational electromagnetics," J. Sci. Comput. **17**(1/4), 405–422 (2002).
36. D. Jiao and J. M. Jin, "An effective algorithm for implementing perfectly matched layers in time-domain finite-element simulation of open-region EM problems," IEEE Trans. Antennas Propagat. **50**(9), 1192–1202 (2002).
37. O. Ramadan, "Auxiliary differential equation formulation: An efficient implementation of the perfectly matched layer," IEEE Microw. Wireless Compon. Lett. **13**(2), 69–71 (2003).
38. T. Rylander and J. M. Jin, "Perfectly matched layer for the time domain finite element method," J. Comput. Phys. **200**(1), 238–250 (2004).
39. N. A. Gondarenko, P. N. Guzdar, S. L. Ossakow, and P. A. Bernhardt, "Perfectly matched layers for radio wave propagation in inhomogeneous magnetized plasmas," J. Comput. Phys. **194**(2), 481–504 (2004).
40. B. Sjögreen and N. A. Petersson, "Perfectly matched layers for Maxwell's equations in second order formulation," J. Comput. Phys. **209**(1), 19–46 (2005).
41. Z. Lou, D. Correia, and J. Jin, "Second-order perfectly matched layers for the time-domain finite-element method," IEEE Trans. Antennas Propagat. **55**(3), 1000–1004 (2007).
42. B. Donderici and F. L. Teixeira, "Conformal perfectly matched layer for the mixed finite element time-domain method," IEEE Trans. Antennas Propagat. **56**(4), 1017–1026 (2008).
43. A. F. Oskooi, L. Zhang, Y. Avniel, and S. G. Johnson, "The failure of perfectly matched layers, and towards their redemption by adiabatic absorbers," Opt. Express **16**(15), 11376 (2008).
44. N. Feng, Y. Yue, C. Zhu, L. Wan, and Q. H. Liu, "Second-order PML: Optimal choice of nth-order PML for truncating FDTD domains," J. Comput. Phys. **285**, 71–83 (2015).
45. K. Duru and G. Kreiss, "Efficient and stable perfectly matched layer for CEM," Appl. Numer. Math. **76**, 34–47 (2014).

Optics EXPRESS

46. E. Bécache, P. Joly, M. Kachanovska, and V. Vinoles, "Perfectly matched layers in negative index metamaterials and plasmas," ESAIM: Proc. **50**, 113–132 (2015).
47. E. Bécache, P. Joly, and M. Kachanovska, "Stable perfectly matched layers for a cold plasma in a strong background magnetic field," J. Comput. Phys. **341**, 76–101 (2017).
48. E. Bécache, P. Joly, and V. Vinoles, "On the analysis of perfectly matched layers for a class of dispersive media and application to negative index metamaterials," Math. Comp. **87**, 2775–2810 (2018).
49. T. Dohnal and T. Hagstrom, "Perfectly matched layers in photonics computations: 1D and 2D nonlinear coupled mode equations," J. Comput. Phys. **223**(2), 690–710 (2007).
50. J. A. Roden and S. D. Gedney, "Convolution PML (CPML): An efficient FDTD implementation of the CFS–PML for arbitrary media," Microw. Opt. Technol. Lett. **27**(5), 334–339 (2000).
51. J. P. Bérenger, "Numerical reflection from FDTD-PMLs: A comparison of the split PML with the unsplit and CFS PMLs," IEEE Trans. Antennas Propagat. **50**(1), 1–11 (2002).
52. J. P. Bérenger, "Application of the CFS PML to the absorption of evanescent waves in waveguides," IEEE Microw. Wireless Compon. Lett. **12**(6), 218–220 (2002).
53. D. Correia and J. M. Jin, "A simple and efficient implementation of CFS-PML in the FDTD analysis of periodic structures," IEEE Microw. Wireless Compon. Lett. **15**(7), 487–489 (2005).
54. D. Appelö, T. Hagstrom, and G. Kreiss, "Perfectly matched layers for hyperbolic systems: General formulation, well-posedness, and stability," SIAM J. Appl. Math. **67**(1), 1–23 (2006).
55. S. D. Gedney and B. Zhao, "An Auxiliary Differential Equation Formulation for the Complex-Frequency Shifted PML," IEEE Trans. Antennas Propag. **58**(3), 838–847 (2010).
56. K. Duru and G. Kreiss, "On the accuracy and stability of the perfectly matched layer in transient waveguides," J. Sci. Comput. **53**(3), 642–671 (2012).
57. F. Pled and C. Desceliers, "Review and Recent Developments on the Perfectly Matched Layer (PML) Method for the Numerical Modeling and Simulation of Elastic Wave Propagation in Unbounded Domains," Archives of Computational Methods in Engineering (2021).
58. U. Köcher and M. Bause, "Variational Space–Time Methods for the Wave Equation," J. Sci. Comput. **61**(2), 424–453 (2014).
59. M. Anselmann and M. Bause, "Numerical Study of Galerkin–Collocation Approximation in Time for the Wave Equation," in *Mathematics of Wave Phenomena*, W. Dörfler, M. Hochbruck, D. Hundertmark, W. Reichel, A. Rieder, R. Schnaubelt, and B. Schörkhuber, eds. (Springer International Publishing, 2020), Trends in Mathematics, pp. 15–36.
60. M. Bause, M. P. Bruchhäuser, and U. Köcher, "Flexible goal-oriented adaptivity for higher-order space-time discretizations of transport problems with coupled flow," Comput. & Math. with Appl. **91**, 17–35 (2021).
61. W. Bangerth, M. Geiger, and R. Rannacher, "Adaptive Galerkin finite element methods for the wave equation," Comput. Methods Appl. Math. **10**(1), 3–48 (2010).
62. G. Matthies and F. Schieweck, "Higher order variational time discretizations for nonlinear systems of ordinary differential equations," Preprint p. 30 (2011).
63. D. Dragna, P. Pineau, and P. Blanc-Benon, "A generalized recursive convolution method for time-domain propagation in porous media," J. Acoust. Soc. Am. **138**(2), 1030–1042 (2015).
64. L. Li, B. Wei, Q. Yang, and D. Ge, "Semi-analytical recursive convolution finite-element time-domain method for electromagnetic analysis of dispersive media," Optik **206**, 163754 (2020).
65. D. Jiao and J.-M. Jin, "Time-domain finite-element modeling of dispersive media," IEEE Microw. Wireless Compon. Lett. **11**(5), 220–222 (2001).
66. D. S. Abraham and D. D. Giannacopoulos, "Dispersive Möbius Transform Finite-Element Time-Domain Method on Graphics Processing Units," IEEE Trans. Magn. **52**(3), 1–4 (2016).
67. A. Akbarzadeh-Sharbaf and D. D. Giannacopoulos, "A Stable and Efficient Direct Time Integration of the Vector Wave Equation in the Finite-Element Time-Domain Method for Dispersive Media," IEEE Trans. Antennas Propag. **63**(1), 314–321 (2015).
68. D. S. Abraham and D. D. Giannacopoulos, "A Convolution-Free Mixed Finite-Element Time-Domain Method for General Nonlinear Dispersive Media," IEEE Trans. Antennas Propag. **67**(1), 324–334 (2019).
69. L. C. Evans, *Partial Differential Equations, Graduate Studies in Mathematics* (American Mathematical Society, 2010).
70. Y. Saad, *Iterative Methods for Sparse Linear Systems* (PWS Publishing Company, 1996).
71. W. Hackbusch, *Multi-Grid Methods and Applications* (Springer, 1985).
72. P. Wesseling, *An Introduction to Multigrid Methods* (Wiley, Chichester, 1991).
73. P. Deuflhard, *Newton Methods for Nonlinear Problems. Affine Invariance and Adaptive Algorithms*, vol. 35 of *Computational Mathematics* (Springer, 2011).
74. P. Deuflhard, *Newton Methods for Nonlinear Problems* (Springer, 2005).
75. D. Arndt, W. Bangerth, B. Blais, M. Fehling, R. Gassmöller, T. Heister, L. Heltai, U. Köcher, M. Kronbichler, M. Maier, P. Munch, J.-P. Pelteret, S. Proell, K. Simon, B. Turcksin, D. Wells, and J. Zhang, "The deal.II library, Version 9.3," J. Numer. Math. **29**(3), 171–186 (2021).
76. L. Berger-Vergiat, C. A. Glusa, J. J. Hu, M. Mayr, A. Prokopenko, C. M. Siefert, R. S. Tuminaro, and T. A. Wiesner, "MueLu user's guide," Tech. Rep. SAND2019-0537, Sandia National Laboratories (2019).

Optics EXPRESS

77. P. V. Gorelik, F. N. C. Wong, D. Kolker, and J.-J. Zondy, "Cascaded optical parametric oscillation with a dual-grating periodically poled lithium niobate crystal," Opt. Lett. **31**(13), 2039 (2006).
78. P. T. Nee and N. C. Wong, "Optical frequency division by 3 of 532nm in periodically poled lithium niobate with a double grating," Opt. Lett. **23**(1), 46 (1998).